Three dimensional efficient meshfree simulation of large deformation failure evolution in soil medium

WANG DongDong[1*], LI ZhuoYa[1], LI Ling[1] & WU YouCai[2]

[1] *Department of Civil Engineering, Xiamen University, Xiamen 361005, China;*
[2] *Karagozian & Case, 2550 N Hollywood Way, Suite 500, Burbank, CA 91505, USA*

An efficient Galerkin meshfree formulation for three dimensional simulation of large deformation failure evolution in soils is presented. This formulation utilizes the stabilized conforming nodal integration, where for the purpose of stability and efficiency a Lagrangian smoothing strain at nodal point is constructed and thereafter the internal energy is evaluated nodally. This formulation ensures the linear exactness, efficiency and spatial stability in a unified manner and it makes the conventional Galerkin meshfree method affordable for three dimensional simulation. The three dimensional implementation of stabilized conforming nodal integration is discussed in details. To model the failure evolution in soil medium a coupled elasto-plastic damage model is used and an objective stress integration algorithm in combination of elasto-damage predictor and plastic corrector method is employed for stress update. Two typical numerical examples are shown to demonstrate the effectiveness of the present method for modeling large deformation soil failure.

meshfree method, three dimensions, stabilized conforming nodal integration, failure evolution, large deformation

1 Introduction

Meshfree methods have experienced substantial development and found rapidly growing applications during the past two decades and the state of art reviews can be found in the refs. [1–4]. Within in the context of meshfree methods the most often employed approximations are the moving least square (MLS) [5] and reproducing kernel (RK) [6] approximants, i.e., the element free Galerkin method and the reproducing kernel particle method. Due to the fact that the MLS/RK approximation is built upon on particles without any necessary topological connectivity, the meshfree methods are very suitable for large deformation and moving boundary problems where the conventional finite element methods encounter sever difficulties in one hand or the other [1, 7]. Nonetheless one major issue which to a large extent blocks the large scale meshfree solutions to practical problems is the relatively low computational efficiency. The high cost of Galerkin meshfree methods owes to the non-polynomial MLS/RK approximation that makes higher order quadrature necessary for domain integration.

To accelerate the meshfree computation salient efforts have been spent in developing lower order stable integration methods. The meshfree nodal integration method was first introduced by Bessil and Belytschko [8] through adding stabilizing terms in the weak form in order to avoid the instability associated with the direct nodal integration. Later on Chen et al. [9, 10] developed an elegant integration algorithm, i.e., the stabilized conforming nodal integration (SCNI) method, for linear and nonlinear problems. This method inherits the high efficiency property associated with

*Corresponding author (email: ddwang@xmu.edu.cn)

the direct nodal integration without introducing any artificial parameters. Moreover, the linear exactness is ensured by the stabilized conforming nodal integration formulation. Subsequently this type of method was further developed to model plate and shell structures where the bending exactness is emphasized [11–16].

As a typical geomaterial, analysis and modeling of soil behavior is fundamentally important for engineering practice. In the meshfree setting, Wu et al. [17] developed a two dimensional Lagrangian meshfree formulation for analysis of geotechnical materials under large deformation condition, where the accuracy and advantage of Galerkin meshfree method for geomechanics problems are fully demonstrated. However, the formulation in [17] employed the Gauss integration rule, which suffers from the low efficiency as stated earlier. Bui et al. [18] employed the method of smoothed particle hydrodynamics to analyze failure of geomaterials, while it is widely known that this method has the obvious disadvantage of tensile instability. In ref. [19] a two dimensional meshfree method based on the stabilized conforming nodal integration was proposed for analyzing large deformation failure of geomaterials. Subsequently, this approach was also generalized to model the rainfall induced slope failure problems under the two dimensional circumstance [20]. In this work, the stabilized conforming nodal integration approach is employed to construct an efficient three dimensional meshfree method for simulation of soil failure with particular reference to large deformation behavior, which is an obvious advantage of the meshfree method.

This paper is organized as follows. The basic equations are summarized in section 2. Section 3 presents the Lagrangian meshfree approximation. The strain smoothing and smoothed nodal gradient are discussed in section 4. Subsequently in section 5 the discrete equations of motion and objective stress update procedure are presented. The numerical demonstration is shown in section 6. Finally, conclusions are drawn in section 7.

2　Basic equations

Consider a soil medium which occupies a bounded physical domain $\mathcal{B}^0$ with boundary $\partial\mathcal{B}^0$ at the initial time $t=0$. A generic material point on the initial configuration $\bar{\mathcal{B}}^0 = \mathcal{B}^0 \cup \partial\mathcal{B}^0$ is denoted by X. After a motion $\boldsymbol{\varphi}(X,t)$, the problem domain referring to the current configuration at time t becomes $\bar{\mathcal{B}} = \mathcal{B} \cup \partial\mathcal{B}$ and the material point X is mapped to the spatial point $x = \boldsymbol{\varphi}(X,t)$. Thus the displacement vector associated with the material point X can be stated as

$$\boldsymbol{u}(X,t) = \boldsymbol{\varphi}(X,t) - X. \tag{1}$$

Therefore, the deformation gradient $\boldsymbol{F}(X,t)$ is given

by

$$\begin{aligned} \boldsymbol{F}(X,t) &= \nabla_X \boldsymbol{\varphi}(X,t) \\ &= \boldsymbol{I} + \nabla_X \boldsymbol{u}(X,t), \end{aligned} \tag{2}$$

where $\nabla_X \equiv \partial/\partial X$ and $\boldsymbol{I}$ is the second order identity tensor.

The rate of deformation tensor $\dot{\boldsymbol{\varepsilon}}$ and spin tensor $\dot{\boldsymbol{w}}$ are defined as

$$\dot{\boldsymbol{\varepsilon}} = [\nabla_x \dot{\boldsymbol{u}} + (\nabla_x \dot{\boldsymbol{u}})^{\mathrm{T}}]/2, \tag{3}$$

$$\dot{\boldsymbol{w}} = [\nabla_x \dot{\boldsymbol{u}} - (\nabla_x \dot{\boldsymbol{u}})^{\mathrm{T}}]/2, \tag{4}$$

where the upper dot denotes the material time derivative.

Within the updated Lagrangian framework the variational statement of the soil motion is

$$\begin{aligned} G(\boldsymbol{\eta}, \boldsymbol{u}) &= \int_{\mathcal{B}} \rho\boldsymbol{\eta} \cdot \ddot{\boldsymbol{u}}\mathrm{d}V + \int_{\mathcal{B}} (\nabla_x \boldsymbol{\eta}) : \boldsymbol{\sigma}\mathrm{d}V - \int_{\mathcal{B}} \boldsymbol{\eta} \cdot \boldsymbol{b}\mathrm{d}V - \int_{\partial\mathcal{B}^t} \boldsymbol{\eta} \cdot \boldsymbol{t}\mathrm{d}S \\ &= 0 \end{aligned} \tag{5}$$

where $\boldsymbol{\eta}$ is the test function, $\ddot{\boldsymbol{u}}$ is the acceleration, ρ and $\boldsymbol{b}$ are the density and body force referring to the current configuration, respectively, $\nabla_x \equiv \partial/\partial x$, $\boldsymbol{\sigma}$ is the nominal Cauchy stress tensor, and t is the surface traction on the natural boundary $\partial\mathcal{B}^t$.

To describe the damage evolution in the soil medium, the strain-based isotropic damage model [21] is employed, where the effective stress tensor $\bar{\boldsymbol{\sigma}}$ is related to the nominal stress tensor $\boldsymbol{\sigma}$:

$$\bar{\boldsymbol{\sigma}} = (1-\zeta)^{-1}\boldsymbol{\sigma}, \tag{6}$$

with ζ being the damage parameter. Here, the following classical damage relationship is employed to update ζ:

$$\zeta = \begin{cases} 0, & \text{if } e_t < e_0, \\ [e_f(e_t - e_0)]/[e_t(e_f - e_0)], & \text{if } e_0 < e_t < e_f, \\ 1, & \text{if } e_t > e_f, \end{cases} \tag{7}$$

where e_t is an equivalent strain measure, i.e., $e_t = \int_0^t \|\dot{\boldsymbol{\varepsilon}}\|\,\mathrm{d}t$. e_0 and e_f are the initial and final damage thresholds.

The plastic behavior of soil is modeled by using the pressure dependent Drucker-Prager law:

$$g(\bar{\boldsymbol{\sigma}}) = \|\mathrm{dev}(\bar{\boldsymbol{\sigma}})\| - \alpha\mathrm{tr}(\bar{\boldsymbol{\sigma}}) - R \leqslant 0, \tag{8}$$

where $\mathrm{dev}(\cdot)$ and $\mathrm{tr}(\cdot)$ are the deviatoric and trace operators, respectively. α and R are material parameters. Note that the plasticity of eq. (8) is formulated via the effective stress tensor and that this approach leads to a very robust elastic-damage predictor and plastic corrector algorithm [21, 22].

3   Lagrangian meshfree approximation

With a Lagrangian version of meshfree approximation, as shown in Figure 1 the problem domain $\bar{\mathcal{B}}_0$ is discretized by a set of material particles $\{X_I\}_{I=1}^{NP}$, and the MLS/RK approximation of displacement $u_i(X,t)$ denoted by $u_i^h(X,t)$ can be expressed as

$$u_i^h(X,t) = \sum_{I=1}^{NP} \Psi_I(X) d_{Ii}(t),\qquad(9)$$

where $\Psi_I(X)$ and $d_{Ii}(t)$ are the MLS/RK shape function and nodal coefficient, respectively. According to the MLS/RK approximation framework [5–7] the shape function $\Psi_I(X)$ takes the following form:

$$\Psi_I(X) = h^{\mathrm{T}}(X_I - X)c(X)\phi_r(X_I - X),\qquad(10)$$

where $\phi_r(X_I - X)$ represents the cubic B-spline Lagrangian kernel function that centers at X_I with a compact support size of r [7]. The three dimensional kernel function can be easily constructed by using tenor product of one dimensional kernel function in each direction. $c(X)$ is an unknown coefficient vector to be determined. $h(X)$ is the n-th order monomial basis vector given by
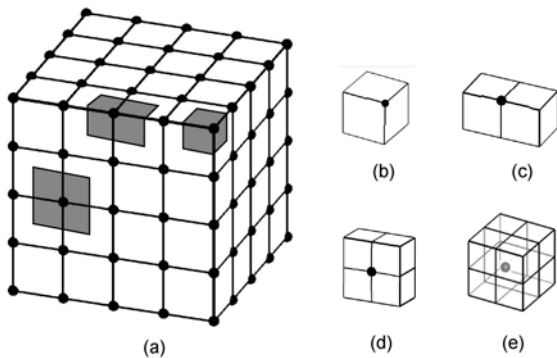
$$h^{\mathrm{T}}(X) = \{1,\ X_1,\ X_2, X_3, X_1^2, \cdots, X_3^n\}.\qquad(11)$$

The position dependent unknown coefficient vector $c(X)$ can be solved through imposing the following n-th order consistent conditions [3]:

$$\sum_{I=1}^{NP} \Psi_I(X) X_{I1}^{p_1} X_{I2}^{p_2} X_{I3}^{p_3}$$
$$= X_1^{p_1} X_2^{p_2} X_3^{p_3},\quad 0 \leqslant p_1 + p_2 + p_3 \leqslant n.\qquad(12)$$

By a vector form eq. (12) becomes

$$\sum_{I=1}^{NP} \Psi_I(X) h(X_I - X) = h(0).\qquad(13)$$

Figure 1 Meshfree discretization and nodal representative domains. (a) Meshfree discretization; (b) corner particle; (c) edge particle; (d) surface particle; (e) interior particle.

Then, substituting eq. (10) into eq. (13) yields

$$c(X) = \mathcal{M}^{-1}(X) h(0),\qquad(14)$$

with $M(X)$ being the moment matrix:

$$\mathcal{M}(X) = \sum_{I=1}^{NP} h(X_I - X) h^{\mathrm{T}}(X_I - X) \phi_r(X_I - X).\qquad(15)$$

Finally the MLS/RK shape function becomes:

$$\Psi_I(X) = h^{\mathrm{T}}(0) \mathcal{M}(X) h(X_I - X) \phi_r(X_I - X).\qquad(16)$$

From the n-th order consistency conditions defined in eq. (12), the following relationship for derivatives can be readily obtained:

$$\sum_{I=1}^{NP} \frac{\partial^{r_1+r_2+r_3}[\Psi_I(X)]}{\partial X_1^{r_1} \partial X_2^{r_2} \partial X_3^{r_3}} X_{I1}^{p_1} X_{I2}^{p_2} X_{I3}^{p_3}$$
$$= \frac{p_1!\, p_2!\, p_3!}{(p_1-r_1)!(p_2-r_2)!(p_3-r_3)!} X_1^{p_1-r_1} X_2^{p_2-r_2} X_3^{p_3-r_3},\qquad(17)$$

where $0 \leqslant (p_1+p_2+p_3), (r_1+r_2+r_3) \leqslant n$. Particularly，the following linear completeness conditions are critically important since they are necessary to get convergent numerical solutions for Galerkin meshfree formulation:

$$\begin{cases} \displaystyle\sum_{I=1}^{NP} \Psi_I(X) = 1, \\[2mm] \displaystyle\sum_{I=1}^{NP} \Psi_I(X) X_{IJ} = X_J, \\[2mm] \displaystyle\sum_{I=1}^{NP} \nabla_{X_J} \Psi_I(X) = 0, \\[2mm] \displaystyle\sum_{I=1}^{NP} \nabla_{X_J} \Psi_I(X) X_{IK} = \delta_{JK}, \end{cases} \quad J,K = \{1,2,3\},\qquad(18)$$

with $\nabla_{X_J} \equiv \partial/\partial X_J$.

4   Strain smoothing and smoothed nodal gradient

To improve computational efficiency and enhance the spatial stability of nodal integration, a smoothing displacement gradient at a generic meshfree particle X_L is defined as [9–15]

$$\nabla_X u_i^h(X_L,t) = \frac{1}{V_L} \int_{\mathcal{B}_L^0} \nabla_X u_i^h(X,t)\mathrm{d}\Omega$$
$$= \sum_{I=1}^{NP} \frac{1}{V_L} \int_{\mathcal{B}_L^0} \nabla_X \Psi_I(X) \mathrm{d}\Omega\, d_{Ii}(t)$$
$$= \sum_{I=1}^{NP} \frac{1}{V_L} \int_{\partial\mathcal{B}_L^0} \Psi_I(X) N(X) \mathrm{d}S\, d_{Ii}(t)$$
$$= \sum_{I=1}^{NP} \tilde{\nabla}_X \Psi_I(X_L) d_{Ii}(t),\qquad(19)$$

where $\mathcal{B}_L^0$ with boundary $\partial \mathcal{B}_L^0$ denotes the nodal representative domain on the initial configuration as shown in Figure 1, V_L is the volume of $\mathcal{B}_L^0$, and N is the outward surface normal of $\partial \mathcal{B}_L^0$. The Lagrangian smoothed nodal gradient $\tilde{\nabla}_X \Psi_I(X_L)$ is given by

$$\tilde{\nabla}_X \Psi_I(X_L) = \frac{1}{V_L} \int_{\partial \mathcal{B}_L^0} \Psi_I(X) N(X) \mathrm{d}S. \tag{20}$$

Thus, the smoothing deformation gradient becomes

$$\tilde{F}_{i,J}(X_L, t) = \delta_{i,J} + \sum_{I=1}^{NP} \tilde{\nabla}_{X_J} \Psi_I(X_L) d_{Ii}(t). \tag{21}$$

Based on the definition of smoothed nodal gradient in eq. (20), one has

$$\sum_{I=1}^{NP} \tilde{\nabla}_{X_J} \Psi_I(X_L) = \frac{1}{V_L} \int_{\partial \mathcal{B}_L^0} \sum_{I=1}^{NP} \Psi_I N_J \mathrm{d}S$$

$$= \frac{1}{V_L} \int_{\partial \mathcal{B}_L^0} N_J \mathrm{d}S$$

$$= 0, \tag{22a}$$

$$\sum_{I=1}^{NP} \tilde{\nabla}_{X_J} \Psi_I(X_L) X_{IK} = \frac{1}{V_L} \int_{\partial \mathcal{B}_L^0} \sum_{I=1}^{NP} \Psi_I X_{IK} N_J \mathrm{d}S$$

$$= \frac{1}{V_L} \int_{\partial \mathcal{B}_L^0} X_K N_J \mathrm{d}S = \frac{1}{V_L} \int_{\mathcal{B}_L^0} X_{K,J} \mathrm{d}\Omega = \delta_{JK}. \tag{22b}$$

Thus, the Lagrangian smoothed gradient also nodally satisfies the linear completeness conditions that are the counterparts of eq. (18):

$$\begin{cases} \sum_{I=1}^{NP} \tilde{\nabla}_X \Psi_I(X_L) = 0, \\ \sum_{I=1}^{NP} \tilde{\nabla}_{X_J} \Psi_I(X_L) X_{IK} = \delta_{JK}. \end{cases} \tag{23}$$

In Figure 2 the conditions in eq. (23) are numerically verified for the meshfree discretization described in Figure 1.

It is also straightforward to show that the smoothed gradient of eq. (20) associated the interior nodes whose kernel supports do not cover the boundary exactly satisfies the following discrete integration constraint which results from
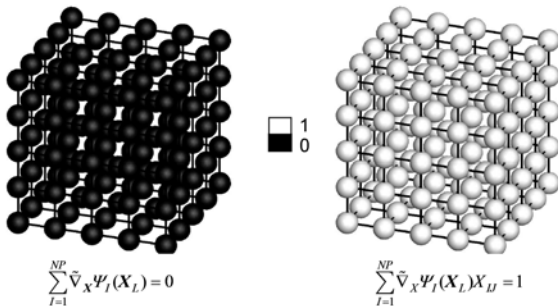
Figure 2   Illustration of linear completeness for smoothed nodal gradient.

the linear exactness condition when arbitrary linear displacement fields based on the initial configuration are prescribed on the boundary:

$$\sum_{L=1}^{NP} \tilde{\nabla}_X \Psi_I(X_L) V_L = 0. \tag{24}$$

With the aid of eq. (21) the spatial smoothed gradient $\tilde{\nabla}_x \Psi_I(X_L)$ can be obtained via the chain rule:

$$\tilde{\nabla}_x \Psi_I(X_L) = [\tilde{\nabla}_X \Psi_I(X_L)] \cdot [\tilde{F}^{-1}(X_L, t)]. \tag{25}$$

5 Discretized equations and stress update procedure

Introducing the MLS/RK approximation of eq. (9) and the smoothed nodal gradients of eqs. (19) and (25) into eq. (5) with a nodal integration gives the following semi-discreitzed equation:

$$r(x) = f^{\text{ext}} - Ma - f^{\text{int}} = 0, \tag{26}$$

with a being the acceleration coefficient vector. The elements of external force vector f^{ext}, mass matrix M, and internal force vector f^{int} are given by

$$f_I^{\text{ext}} = \sum_{L=1}^{NP} \Psi_I(X_L) b_0(X_L) V_L + \sum_{K=1}^{NB} \Psi_I(X_K) t_0(X_K) S_K, \tag{27}$$

$$M_{IJ} = I \sum_{L=1}^{NP} \rho_0 \Psi_I(X_L) \Psi_J(X_L) V_L, \tag{28}$$

$$f_I^{\text{int}} = \sum_{L=1}^{NP} \tilde{B}_I^T(X_L) \Theta(X_L) \det(\tilde{F}(X_L)) V_L, \tag{29}$$

$$\tilde{B}_I = \begin{bmatrix} \tilde{\nabla}_x \Psi_I & 0 & 0 \\ 0 & \tilde{\nabla}_y \Psi_I & 0 \\ 0 & 0 & \tilde{\nabla}_z \Psi_I \\ \tilde{\nabla}_y \Psi_I & \tilde{\nabla}_x \Psi_I & 0 \\ \tilde{\nabla}_z \Psi_I & 0 & \tilde{\nabla}_x \Psi_I \\ 0 & \tilde{\nabla}_z \Psi_I & 0 \end{bmatrix}, \tag{30}$$

$$\Theta = \{\sigma_{xx} \quad \sigma_{yy} \quad \sigma_{zz} \quad \sigma_{xy} \quad \sigma_{xz} \quad \sigma_{yz}\}^T, \tag{31}$$

where b_0, t_0 and ρ_0 are the body force, density and traction referring to the initial configuration, respectively.

Within the time domain the given time interval $[0, T]$ is partitioned into a set of sub-intervals $[t_m, t_{m+1}]$, and $\Delta t = t_{m+1} - t_m$. If one-step method is used the solutions at t_m are assumed to be known and the solutions at t_{m+1} are to be solved. Here, through employing the central difference algorithm [23] the final discretized equations corresponding to eq. (26) are

$$Ma_{m+1} = f_{m+1}^{ext} - f_m^{int}, \qquad (32)$$

$$d_{m+1} = d_m + v_m \Delta t + a_m (\Delta t)^2 / 2, \qquad (33)$$

$$v_{m+1} = v_m + (a_m + a_{m+1}) \Delta t / 2, \qquad (34)$$

where v_m denotes the velocity coefficient vector at t_{m+1}.

To properly evaluate the internal force in eq. (32) in case of large deformation, the stress σ has to be objectively integrated based on σ_m to obtain σ_{m+1}. In this study the objective stress integration method developed by Hughes and Winget [24] based on the Jaumman rate is used in combination with the elasto-damage and plasticity operator splitting algorithm proposed by Simo and Ju [21]. The stress integration procedure within the context of strain-driven formulation is detailed in Figure 3, where Δu_{m+1} is the displacement increment in the time interval Δt, $x_{m+1/2} = x_m + (\Delta u_{m+1})/2$, C is the fourth order elasticity tensor, and K and μ are the bulk modulus and shear modulus, respectively.
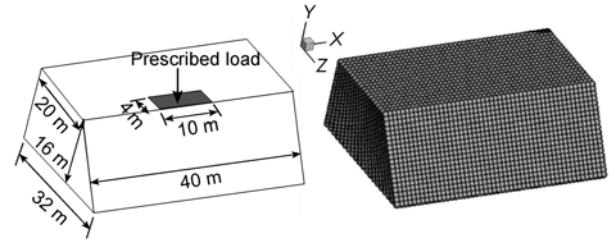
6 Numerical examples

Two typical soil slopes as shown in Figures 4 and 5 are considered in this study. The geometric information for both
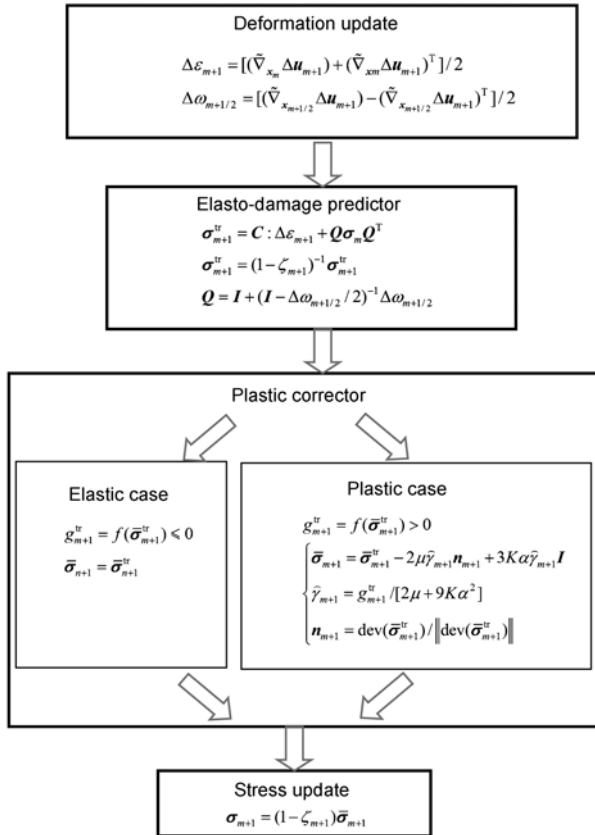
Figure 3 Objective stress update procedure for large deformation elasto-plastic damage modeling.
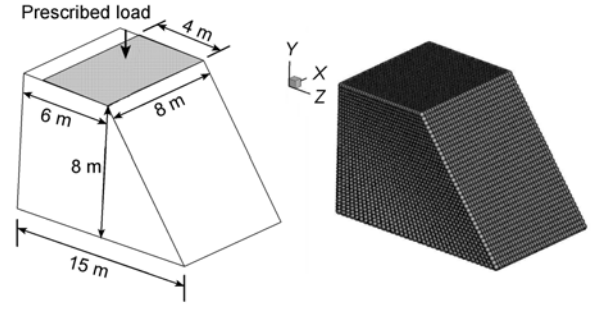

Figure 4 Problem statement and meshfree discretization for slope I.

Figure 5 Problem statement and meshfree discretization for slope II.

slopes is also described in Figures 4 and 5. The material properties for both slopes are taken: bulk modulus K=27.4 MPa, shear modulus μ=9.15 MPa, density ρ_0= 1880 kg/m³, damage initial and final thresholds e_0=0.02 and e_f=5, and plastic parameters α=0.07 and R=0.19 MPa. Both problems are subject to fixed conditions on the bottom surface and three other surrounding surfaces have one-directional fixed condition along their corresponding surface normal vectors, respectively. Meanwhile both slopes are loaded by prescribed vertical displacements at the indicated loading area as shown in Figures 4 and 5. The total uniformly prescribed vertical displacements for slopes I and II are 1m and 2 m, respectively. The loading rates are 10^{-2} m/s and 2×10^{-2} m/s for problems I and II.

The meshfree discretizations for slopes I and II are also plotted in Figures 4 and 5. The numbers of meshfree particles for slopes I and II are 52022 and 48672, respectively. The MLS/RK shape function is constructed by using the linear basis and the normalized kernel support of the cubic B-spline function is set to be 1.5. The time step is selected as 10^{-3} s. The progressive failures of slopes I and II are shown in Figures 6 and 7. In Figure 6, a major shear band which is consistent with conventional slope failure pattern [25] is first gradually activated while a second crossing shear band also starts to grow as the load continues to increase. Consequently, complex branched shear bands are formed and they are responsible for the soil failure. Note that the loading in Figure 6 is invariant along the y direction but this is not the case for the problem shown in Figure 7. Since the loading is applied to a small portion of the upper surface as indicated in Figure 7, the shear band which forms
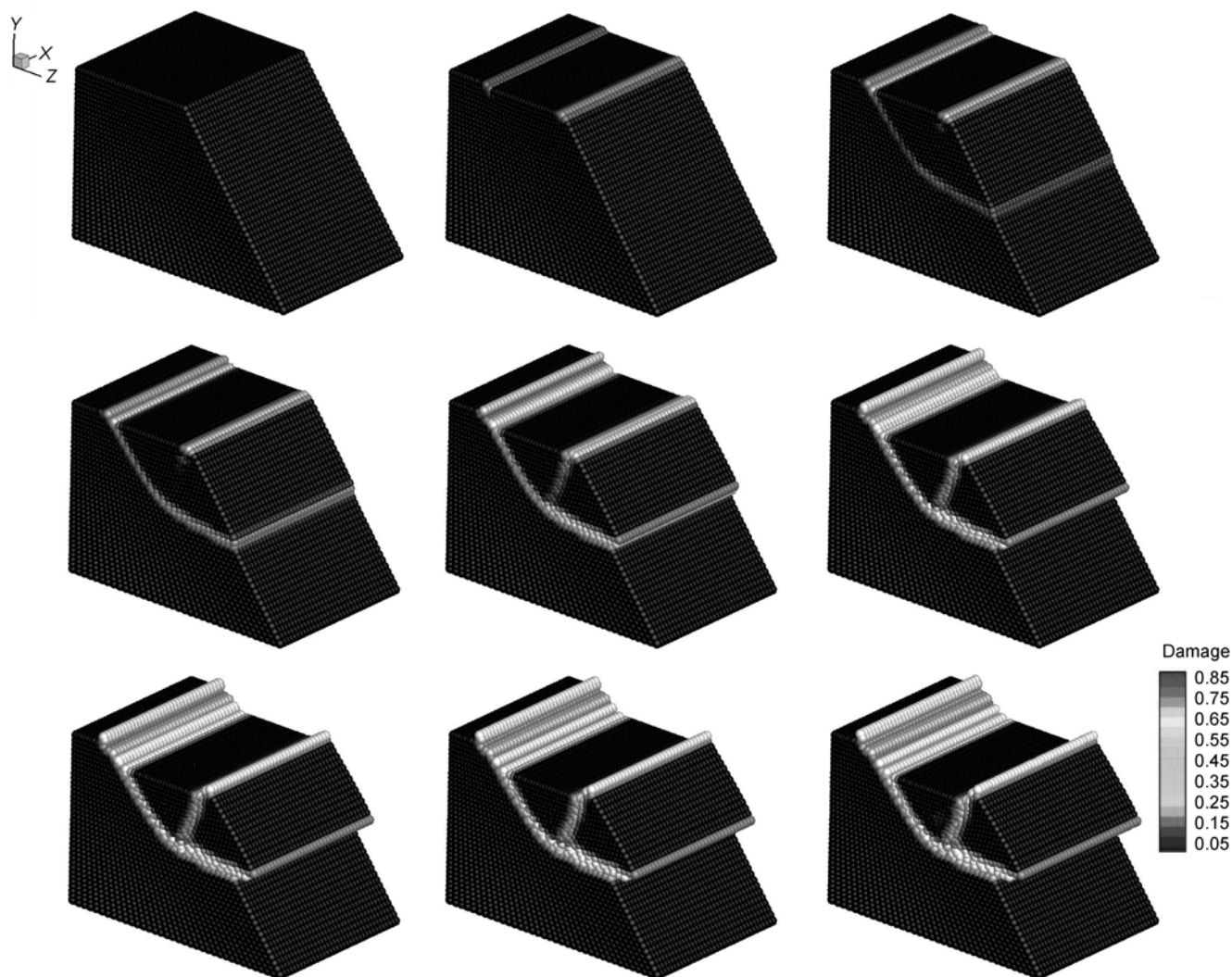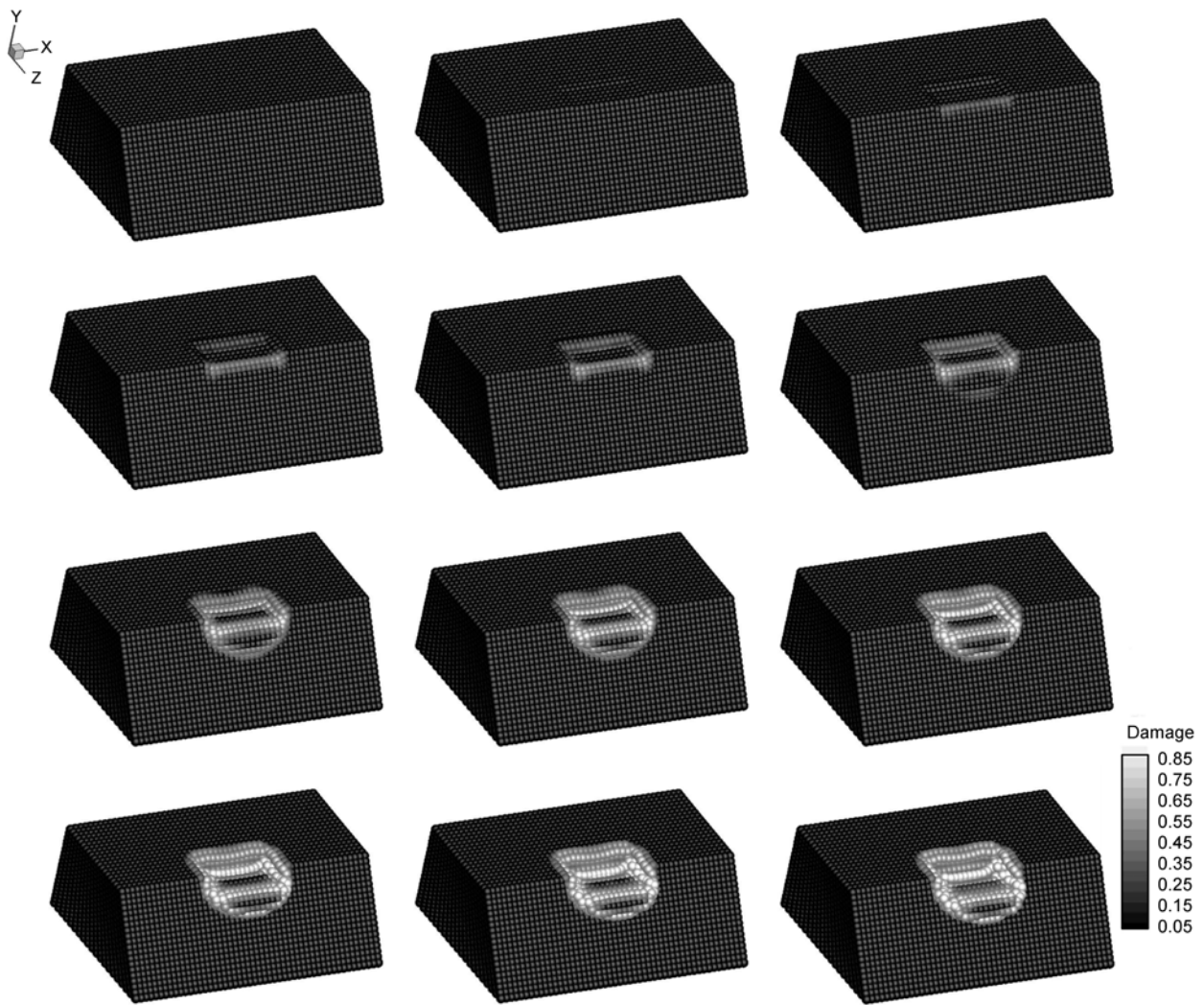
Figure 6   Progressive configurations of failure evolution in slope I.

the sliding surface has a complicated spatial geometry and near the shear band excessive deformation occurs as illustrated by the damage distribution listed in Figure 7. Meanwhile, the detailed displacement and equivalent stress results of the right half model for both problems are depicted in Figures 8 and 9. As a whole, the numerical results for both problems do show that the proposed method is very effective for simulating the complex large deformation soil failure process without requiring re-meshing.

7   Conclusions

A three dimensional updated Lagrangian Galerkin meshfree formulation with improved computational efficiency was presented for the failure analysis of soil medium. This nonlinear meshfree formulation is featured by the Lagrangian stabilized conforming nodal integration method, where the low cost nature of nodal integration approach is kept while the spatial stability is ensured, which is not the case for the direct nodal integration. The stabilized conforming nodal integration is formulated through the gradient smoothing within a nodal representative domain. It was shown that the Lagrangian smoothed nodal gradients also meet the discrete linear completeness conditions. The time dimension is discretized by the explicit central difference algorithm. The initiation and propagation of failure in soils is modeled by the coupled constitutive equations of isotropic damage and Drucker-Prager plasticity. This coupled large deformation constitutive behavior is efficiently treated by the elsto-damage predictor and plastic corrector approach in combination with the objective stress integration. Detailed three dimensional equations were given for the proposed formulation. Numerical results evinced that the present method is very effective in modeling the complex failure mechanism of soil medium.

Figure 7   Progressive configurations of failure evolution in slope II.
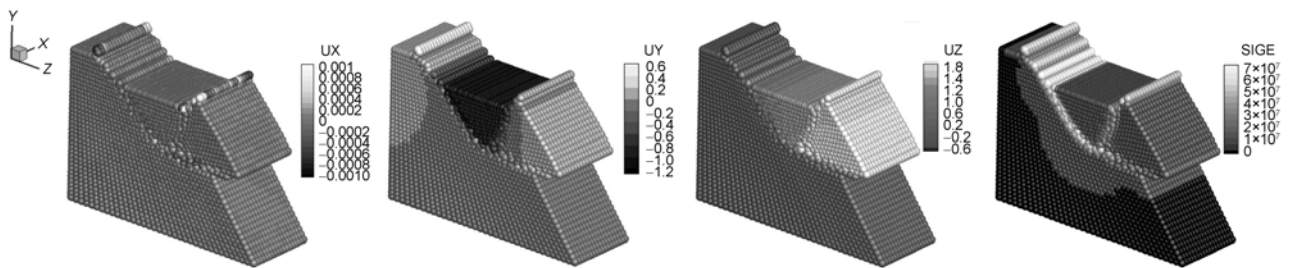
Figure 8   Displacements and equivalent stresses of the right half model for slope I. (a) u_x; (b) u_y; (c) u_z; (d) σ_{eq}.
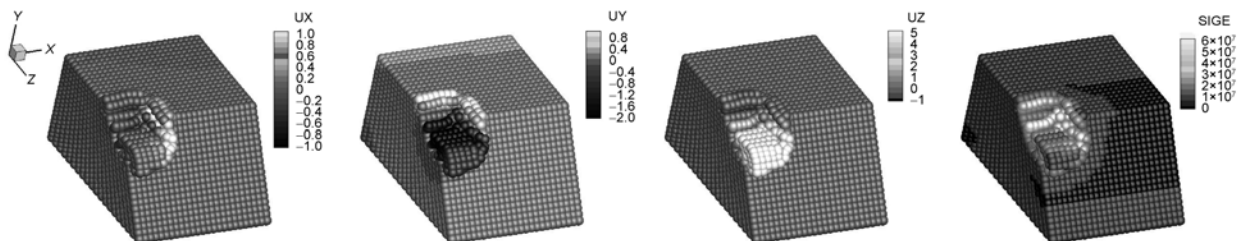
Figure 9   Displacements and equivalent stresses of the right half model for slope II. (a) u_x; (b) u_y; (c) u_z; (d) σ_{eq}.

1   Belytschko T, Kronggauz Y, Organ D, et al. Meshless methods, an overview and recent developments. Comput Method Appl M, 1996, 139: 3–47

2   Zhang X, Liu Y. Meshless Methods. Beijing: Tsinghua Press, 2004

3   Li S, Liu W K. Meshfree and Particle Methods. Berlin: Springer-Verlag, 2004

4   Liu G R. Meshfree Method: Moving beyond the Finite Element Method (2nd edition). CRC Press, 2009

5   Belytschko T, Lu Y Y, Gu L. Element-free Galerkin methods. Int J Numer Meth Eng, 1994, 37: 229–256

6   Liu W K, Jun S, Zhang Y F. Reproducing kernel particle methods. Int J Numer Meth Eng, 1995, 20: 1081–1106

7   Chen J S, Pan C, Wu C T, et al. Reproducing kernel particle methods for large deformation analysis of nonlinear structures. Comput Method Appl M, 1996, 139: 195–227

8   Beissel S, Belytschko T. Nodal integration of the element-free Galerkin method. Comput Method Appl M, 1996, 139: 49–74

9   Chen J S, Wu C T, Yoon S, et al. A stabilized conforming nodal integration for Galerkin meshfree methods. Int J Numer Meth Eng, 2001, 50: 435–466

10   Chen J S, Yoon S, Wu C T. Nonlinear version of stabilized conforming nodal integration for Galerkin meshfree methods. Int J Numer Meth Eng, 2002, 53: 2587–2615

11   Wang D, Chen J S. Locking-free stabilized conforming nodal integration for meshfree Mindlin-Reissner plate formulation. Comput Method Appl M, 2004, 193: 1065–1083

12   Wang D, Chen J S. A locking-free meshfree curved beam formulation with the stabilized conforming nodal integration. Comput Mech, 2006, 39: 83–90

13   Wang D, Dong S B, Chen J S. Extended meshfree analysis of trans-verse and inplane loading of a laminated anisotropic plate of general planform geometry. Int J Solids Struct, 2006, 43: 144–171

14   Wang D, Chen J S. A Hermite reproducing kernel approximation for thin plate analysis with sub-domain stabilized conforming integration. Int J Numer Meth Eng, 2008, 74: 368–390

15   Wang D, Wu Y. An efficient Galerkin meshfree analysis of shear deformable cylindrical panels. Interact Multiscale Mech, 2008, 1: 339–355

16   Wang D, Lin Z. Free vibration analysis of thin plates using Hermite reproducing kernel Galerkin meshfree method with sub-domain stabilized conforming integration. Comput Mech, 2010, 46: 703–719

17   Wu C T, Chen J S, Chi L, et al. Lagrangian meshfree formulation for analysis of geotechnical materials. J Eng Mech-ASCE, 2001, 127: 440–449

18   Bui H H, Fukagawa R, Sako K, et al. Lagrangian meshfree particles method (SPH) for large deformation and failure flows of geomaterial using elastic-plastic soil constitutive model. Int J Numer Anal Meth Geomech, 2008, 32: 1537–1570

19   Wang D. Large deformation dynamic meshfree simulation of damage and failure in geomaterials. Key Eng Mater, 2006, 324–325, 141–144

20   Wang D, Li L. Efficient meshfree large deformation simulation of rainfall induced soil slope failure. In: Proceedings of the 2nd International Symposium on Computational Mechanics. Hong Kong and Macao, 2009

21   Simo J C, Ju J W. Strain and stress-based continuum damage models-I formulation. Int J Solids Struct, 1987, 23: 821–840

22   Ju J W. On energy-based coupled elastoplastic damage theories: Constitutive modeling and computational aspects. Int J Solids Struct, 1989, 25: 803–833

23   Hughes T J R. The Finite Element Method: Linear Static and Dynamic Finite Element Analysis. Mineola, NY: Dover Publications, 2000

24   Hughes T J R, Winget J M. Finite rotation effects in numerical integration of rate constitutive equations arising in large deformation analysis. Int J Numer Meth Eng, 1980, 15: 1862–1867

25   Zheng Y, Chen Z, Wang G, et al. Engineering Treatment of Slope and Landslide. Beijing: China Communications Press, 2007